nature materials

Article

https://doi.org/10.1038/s41563-026-02492-y

A molten-salt dispersion of lanthanides at the atomic scale

Received: 14 December 2024

Accepted: 13 January 2026

Published online: 19 February 2026

Check for updates

Haoyuan Wang[1,2], Chunxiao Liu[1], Yuan Ji[1], Hongliang Zeng[1], Sunpei Hu[2], Xinyan Zhang[1,2], Qisheng Zeng[1], Jiawei Li[1], Qinglong Gao[1], Yao Zhang[2], Jie Zeng[2], Xu Li[1], Tingting Zheng[1], Qiu Jiang[1] & Chuan Xia[1]

Lanthanide (Ln) elements have distinctive electronic structures and chemical behaviours that can be used to tune electrocatalytic performance when they are introduced as isolated atomic modifiers. However, their broader use remains limited because their high reactivity and ultralow reduction potentials make it difficult to develop general synthesis strategies that can atomically disperse Ln atoms on diverse substrates. Here we develop a molten-nitrite method that yields Ln single-atom catalysts, permitting the atomic isolation of multiple lanthanides on various supports, including metals, metal oxides and carbon materials. Mechanistic insights obtained from systematic control experiments indicate that Ln single-atom catalyst formation in molten nitrites is dictated by three factors: the Lux–Flood basicity effect, mass-diffusion resistance and molten-salt shielding. As a demonstration, Dy_1/Pt shows an overpotential of 20 mV at a current density of −10 mA cm^{-2} in 0.5-M H_2SO_4 for acidic hydrogen evolution, which is superior to commercial Pt/C catalysts. This work establishes a framework for synthesizing Ln single-atom catalysts and positions molten-nitrite systems as a versatile platform for electrocatalyst synthesis.

Lanthanides (Ln(s)) have garnered growing attention in catalytic applications because of their ability to offer unique electronic properties that influence reaction mechanisms in ways that traditional catalysts cannot[1]. Their intricate electronic structures, which feature partially filled 4*f* orbitals and high coordination numbers[2], provide a distinct capacity to manipulate reaction pathways and catalytic activity. This, combined with their strong affinity for oxygen[3,4] and large atomic radius[5,6], endows them with the special interactions with a diverse array of substrates and reactants[7–9], thereby increasing their ability to stabilize intermediates and reduce activation barriers in electrocatalytic processes. In particular, when Ln(s) are atomically dispersed, their electronic and geometric environments can be precisely defined, resulting in the uniform and efficient modulation of key electrocatalytic parameters such as activity, selectivity and stability. For example, the oxophilic isolated Ln sites on the Pt surface can substantially increase the strength of absorbed OH^- during the methanol oxidation process[10] or hydrogen oxidation reaction[3], which can effectively mitigate the CO poisoning effect. Additionally, the distinct spin–orbit coupling effects of isolated Ln(s) can contribute to the stabilization of coordinated lattice oxygen, thereby preserving the high valence states of adjacent elements during electroreduction[11,12]. This strategy has been effectively used to increase the conversion of CO_2 to value-added C_{2+} products in Cu-based catalysts.

Unfortunately, current synthesis protocols for doping Ln(s) at the atomic scale face considerable challenges[1,13]. Wet-chemical methods, including the sol–gel protocol, electrodeposition, hydrothermal synthesis and impregnation methods, are the most widely reported techniques that have been effectively and economically applied to synthesize various single-atom catalysts (SACs) with complex components. Unfortunately, when extended to Ln-based materials, the

[1]School of Materials and Energy, University of Electronic Science and Technology of China, Chengdu, People's Republic of China. [2]Hefei National Research Center for Physical Sciences at the Microscale, University of Science and Technology of China, Hefei, People's Republic of China.
e-mail: chuan.xia@uestc.edu.cn

standard reduction potential of Ln(s), typically lower than −2.3 V versus the standard hydrogen electrode, is substantially below the dissociation thermodynamic potential of water. This discrepancy impedes the direct reduction of the precursor and further deposition processes in aqueous media. The ultralow reduction potential of Ln(s) also makes them highly susceptible to oxidation, which can interfere with the alloying process when combined with less-reactive metals. Additionally, the discrepant nucleation rates, atomic radius divergence, and special bonding performance of *f* orbitals between Ln(s) and other metals can lead to phase separation during wet-chemical methods[14]. To atomically disperse Ln(s) into host substrates, complicated procedures, including physical metallurgy[15], film deposition[6], multistep complex synthesis[3,16] or co-reduction with dangerous agents[17,18], have been used in previous works. These approaches often face challenges for large-scale production because of their intricate procedures or high costs. Moreover, most studies have reported only the dispersion of isolated Ln(s) over oxides or carbon-based materials, and straightforward synthesis strategies for dispersing Ln(s) onto metallic substrates are lacking. This gap hinders their broader applications and practical use[19,20].

In this study, we introduce a general nitrites-based molten-salt method, which demonstrates broad applicability for isolating various Ln elements across different oxides and metallic substrates. Using dysprosium (Dy) as a representative example, we demonstrated the dispersion of Ln(s) onto a range of substrates, including non-noble metals with varying valences (for example, Cu, Cu_2O and CuO), noble metals (Pt, Rh and Ir) and a series of potential substrates (Y_2O_3, ZnO, Pd, AlO_x, RuO_2, SnO_2, FeO_x, Mn_3O_4 and commercial carbon black). We investigated the driving force underlying nanocrystal growth and identified three critical factors essential for the effective application of our molten-nitrite system: high Lux–Flood (L–F) basicity, high mass-diffusion resistance and the molten-salt-shielding effect. Furthermore, we confirmed the versatility of the method for different Ln(s) and its effectiveness in the co-doping of four single-atom Ln(s). As a demonstration, the Dy_1/Pt catalyst produced using this method exhibited enhanced activity and stability in the hydrogen evolution reaction (HER) under acidic conditions.

Synthesis and characterization of Dy_1/CuO, Dy_1/Cu_2O and Dy_1/Cu

The protocol of our molten-nitrite method is illustrated in Fig. 1a. To showcase the effectiveness of the synthesis method, we selected Dy as a representative element to be doped over three different Cu substrates (Cu, Cu_2O and CuO). Situated in the middle of the Ln series, Dy exemplifies the typical properties of Ln(s), including its ionic radius, multiple oxidation states and partially filled 4*f* orbitals. Cu, which has multiple valences and notable chemical reactivity, is chosen as a representative non-noble metal substrate. In addition, Cu is one of the most widely applied elements in electrocatalysis, including the CO_2 reduction reaction[21], CO reduction reaction[22], nitrogen reduction reaction[23], nitrate reduction reaction[24] and 5-hydroxymethylfurfural conversion reaction[25]. In the synthesis process, stoichiometric ratios of nitrates of Dy and Cu are mixed in a small volume of aqueous solution (Methods). The resulting concentrated solution with uniformly dispersed ions, denoted as the Dy–Cu precursor, was then directly injected into molten nitrites (eutectic $NaNO_2$–KNO_2). In this process, the Dy–Cu precursor undergoes ultrafast evaporation, and the precursor ions quickly react with the molten nitrites. After the reaction, the generated Dy_1/CuO nanoparticles (NPs) (Supplementary Fig. 1a) were conveniently washed with water to remove nitrites without any other complex operation. Note that in this work, the subscript '1' in notations such as Dy_1/CuO denotes that Dy exists in a single-atom form, not in a stoichiometric ratio. By simply substituting copper citrate for copper nitrate in the precursor, we can alter the valence of the resulting Cu oxides to +1, denoted as Dy_1/Cu_2O (Supplementary Fig. 2a). Finally, Dy_1/Cu (Supplementary Fig. 3a) can be further generated by directly reducing Dy_1/CuO via an in situ cathodic process, which is identical to our previous work on the synthesis of Pb_1Cu (ref. 26).

Figure 1b–g shows the dispersion of single Dy atoms over all three different Cu substrates. The powder X-ray diffraction (XRD) patterns of Dy_1/CuO, Dy_1/Cu_2O and Dy_1/Cu align with the XRD patterns of the substrates, without agglomerated Dy species (Supplementary Figs. 1b, 2b and 3b). X-ray photoelectron spectroscopy and Cu Auger spectroscopy confirmed that the surfaces of Dy_1/CuO and Dy_1/Cu_2O were dominated by Cu^{2+} (Supplementary Fig. 1c,d) and Cu^+ (Supplementary Fig. 2c,d), respectively. The prevalence of Cu^+ on the Dy_1/Cu surface (Supplementary Fig. 3c,d) is attributed to the oxidation of the nanocrystal Cu in air[27]. The uniform atomic dispersion of Dy atoms in Dy_1/CuO (Fig. 1b,c), Dy_1/Cu_2O (Fig. 1d,e) and Dy_1/Cu (Fig. 1f,g) was confirmed via high-angle annular dark-field scanning transmission electron microscopy (HAADF-STEM) combined with energy-dispersive X-ray spectroscopy (EDS).

Furthermore, X-ray absorption near-edge structure (XANES) and extended X-ray absorption fine structure (EXAFS) analyses were used to investigate the valence state and coordination environment of Dy. Specifically, the X-ray absorption fine structure spectrum of Dy_1/Cu was collected under a consistent cathodic potential (−1.2 V versus a reversible hydrogen electrode (RHE), which is consistent with the synthesis conditions). Compared with metallic Dy and Dy_2O_3, the XANES results reveal higher white-line peaks at the Dy L_3 absorption edge in each sample, indicating the lower occupation of *d* orbitals and suggesting a higher oxidation state of the Dy sites (Supplementary Fig. 4). The EXAFS spectrum shows a peak corresponding to Dy–O at approximately 1.96 Å (Fig. 1h). The absence of Dy–Dy signals at approximately 3.34–3.40 Å suggested the monodispersion of Dy atoms within CuO and Cu_2O. The predominant Dy–O signal in Dy_1/Cu indicates that Dy ions with a positive charge are anchored to Cu and surrounded by O atoms, even during reduction conditions. Under varying applied potentials, the XANES and EXAFS spectra of Dy exhibit negligible absorption edge shifts (Supplementary Fig. 5) and the presence of Dy–O bonds (Supplementary Fig. 6), which can be attributed to the ultralow thermodynamic reduction potential of Ln elements[12] (approximately −2.30 V versus standard hydrogen electrode). In addition, wavelet-transform X-ray absorption fine structure supported the microstructure of single Dy atoms by considering both *k*- and *R*-space information. Only strong signals ascribed to Dy–O coordination are present in Dy_1/CuO, Dy_1/Cu_2O and Dy_1/Cu (Supplementary Fig. 7).

Synthesis mechanisms in molten nitrites

The generation of Dy SACs on Cu-based substrates reveals the versatility of our method for isolating Ln atoms over substrates. However, studies addressing the intrinsic reaction mechanisms from both thermodynamic and kinetic perspectives in this domain are relatively scarce. In contrast to conventional wet-chemical methods, molten salts exhibit deviations from the Arrhenius ionization behaviour observed in aqueous phases, providing a distinct chemical environment. Consequently, we conducted a series of detailed control experiments with molten nitrites to investigate the formation mechanisms of Dy SACs. As discussed below, we summarize three major mechanisms that dominate this process: accelerated nucleation via the L–F acid–base effect (Fig. 2a), controlled growth via the mass-diffusion resistance effect (Fig. 2b) and thermodynamic stabilization through the molten-salt-shielding effect (Fig. 2c).

L–F acid–base effect

The most widely accepted model to describe the growth of NPs in liquid media is the LaMer mechanism proposed in 1950 (ref. 28), which effectively explains NP nucleation and growth. The nucleation dynamics within the LaMer model reveal a critical understanding of our experimental phenomenon (Supplementary Fig. 8 and Supplementary Note 1). As demonstrated in the experiments, the injection of the Dy–Cu

https://doi.org/10.1038/s41563-026-02492-y

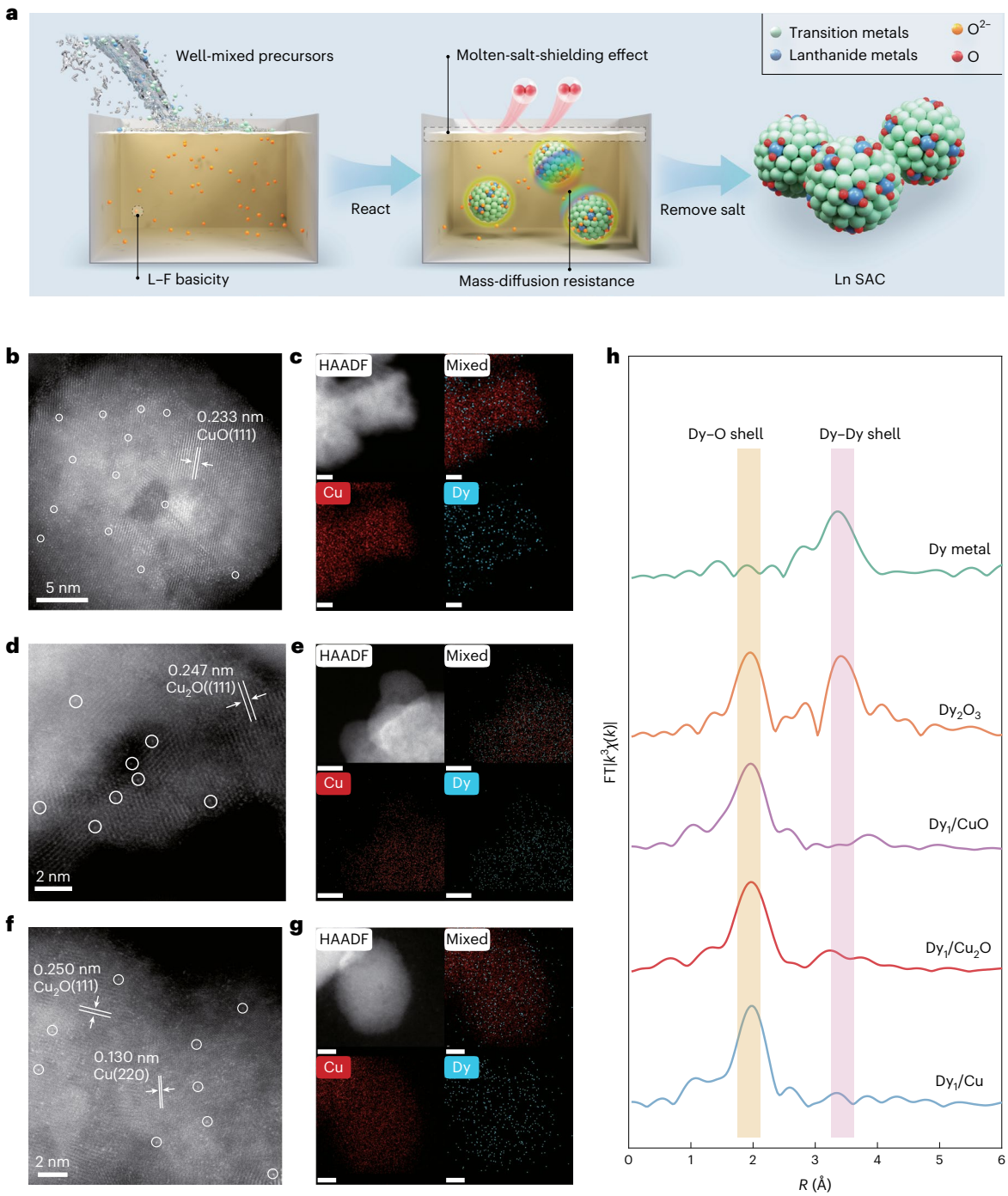

Fig. 1 | Generation of single Dy atoms over various Cu-based substrates. **a**, Schematic of the synthesis process in molten nitrites. **b**–**g**, HAADF-STEM images of atomically dispersed Dy atoms on CuO (**b**), Cu_2O (**d**) and Cu (**f**). The corresponding EDS mapping results are shown for CuO (**c**), Cu_2O (**e**) and Cu (**g**), precluding the presence of aggregated Dy species. Scale bars, 5 nm (**c**,**g**), 10 nm (**e**). **h**, EXAFS at the Dy L_3 edge of Dy_1/CuO, Dy_1/Cu_2O and Dy_1/Cu. Dy_1/Cu was measured during an in situ cathodic reduction. Dy metal and Dy_2O_3 are shown as references. FT, Fourier transform.

precursor into molten nitrites triggered a rapid reaction within seconds, corresponding to the burst nucleation process. By contrast, chemically analogous molten nitrates led to very sluggish nucleation kinetics for Cu^{2+}, together with nearly chemical inertness towards Dy^{3+} (Supplementary Table 1 and Supplementary Note 2). Thermogravimetric analysis revealed substantially lower nucleation temperature thresholds in molten nitrites than in molten nitrates. Both Cu^{2+} and Dy^{3+} display mass-loss peaks below 200 °C in molten nitrites, whereas molten nitrates require approaching 300 °C and 400 °C for Cu^{2+} and Dy^{3+}, respectively (Supplementary Fig. 9 and Supplementary Note 3).

We attribute these nucleation temperature thresholds to the superior L–F basicity (Supplementary Note 4). According to previous reports[29], the formation of a metal oxide requires adequate dissociative O^{2-}, which can be supplied by elevating the temperature or using different oxysalts (as evidenced by the thermogravimetric experiments discussed above). For a quantitative investigation, we used CO_2 as the probe molecule to comparatively study the L–F basicity discrepancy between molten nitrites and nitrates. A quantitative CO_2 fixation experiment revealed that molten nitrites exhibit two orders of magnitude stronger L–F basicity than molten

https://doi.org/10.1038/s41563-026-02492-y

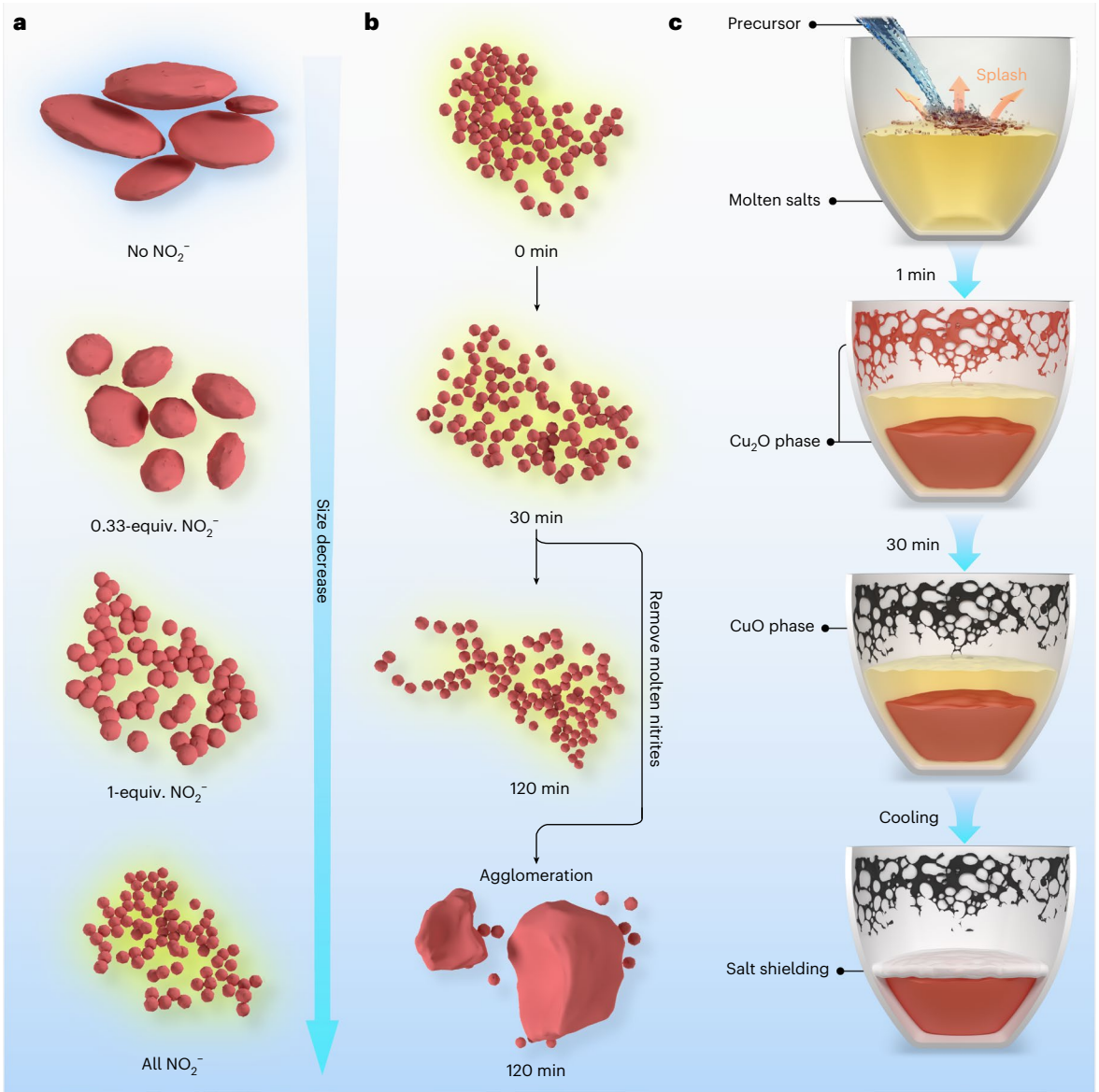

Fig. 2 | Three synthesis mechanisms in molten nitrites. a, L–F acid–base effect: by increasing the equivalent (equiv.) of nitrites in molten salts, the size variation of the obtained products can be determined. The L–F basicity in each molten salt increases as the size of the products decreases. **b**, Mass-diffusion resistance effect: by increasing the holding time of Dy_1/CuO within molten nitrites at 400 °C, the interparticle performance of the obtained products can be evaluated. The molten nitrites inhibited agglomeration during the annealing process. **c**, Molten-salt-shielding effect: schematic of the molten-salt-shielding effect. When the precursor is introduced, Dy_1/Cu_2O with a cuprite phase is immediately generated. After annealing, the Cu_2O phase splashed among the crucible wall is oxidized to the CuO phase, whereas the Cu_2O phase immersed in molten salts is maintained.

nitrates, directly explaining their different nucleation behaviours (Supplementary Note 5).

We propose that the initial nucleation step depends on the O^{2-} concentration, where a high O^{2-} concentration in molten nitrites induces instantaneous supersaturation, generating smaller NPs via burst nucleation according to classic nucleation theory (Supplementary Note 6). For verification, we introduced the Dy–Cu precursor into molten nitrates with tunable L–F basicity via the introduction of $NaNO_2$. Transmission electron microscopy (TEM) images demonstrated that the size of the generated NPs decreased as the L–F basicity increased (Supplementary Fig. 10), which was cross-verified by the broadened CuO(111) peak in the XRD patterns (Supplementary Fig. 11).

The reason why Dy is homogeneously dispersed within the CuO lattice can also be explained. We conclude that the strong L–F basicity of molten nitrites ensures the even dispersal of Ln(s) among CuO. The EDS mapping of the sample generated in molten nitrates revealed the absence of Dy signals (Supplementary Fig. 12), which corresponds to the phenomenon of monitoring the residual ions in molten salts (Supplementary Note 2). In this case, the different acidities of Cu^{2+} and Dy^{3+} undergo sequential nucleation in molten salts with low L–F basicity, culminating in phase separation[30]. By contrast, the molten nitrites in our design provide a much greater L–F basicity to accelerate the nucleation kinetics[31], which provides a non-equilibrium nucleation environment for the co-nucleation of Dy and Cu species[32]. Hence, the homogeneous mixture of the Dy–Cu precursor quickly reacts with excess O^{2-} in molten nitrites. The ultrafast nucleation process entraps Dy within the CuO matrix before other side reactions, facilitating the synthesis of Dy_1/CuO.

Mass-diffusion resistance effect

After the generation of nuclei, stage III of the LaMer model dominates (Supplementary Note 1), which describes the diffusion-controlled

growth of the as-generated nanocrystals. In this stage, Ostwald ripening and particle collision–coalescence occur due to the high surface energy of the newly formed NPs[33], inducing complex structural evolution and the collapse of fine features. To investigate the growth performance in molten salts, we further prolonged the aging time of the synthesis in molten nitrites/nitrates. As indicated by the TEM images and the normalized full-width at half-maximum of the XRD peaks, the CuO NP size of the molten nitrates intensively increased after 120 min of holding (Supplementary Figs. 13a–c and 14a), whereas it only slightly increased in the nitrites (Supplementary Figs. 13d–f and 14b). This discrepancy is attributed to the low Cu^{2+} saturation concentration in molten nitrites, which effectively suppresses the Cu^{2+} dissolution–deposition equilibrium during the Ostwald ripening process (Supplementary Note 7).

Typically, NPs tend to undergo irreversible agglomeration during the annealing step (Supplementary Fig. 15). However, molten nitrites impede this process (Supplementary Fig. 13d–f). Compared with conventional solid-state reactions, the viscous nature of the molten salts effectively hinders particle collision and coalescence[34], thereby resulting in a lower degree of aggregation. To validate the relationship between viscosity and particle agglomeration, we conducted the same aging experiment using modified molten nitrites with high viscosity (KNO_2–$NaNO_2$, molar ratio of 9:1). The composition–viscosity relationship is thoroughly discussed in Supplementary Fig. 16 and Supplementary Note 8 based on the phase diagram (Supplementary Fig. 17) and the Arrhenius equation[35]: near the melting point (T_m), molten salts exhibit higher viscosity. Consequently, negligible particle growth or agglomeration occurred during the aging process in this system, as evidenced by the TEM images (Supplementary Fig. 18) and the full-width at half-maximum comparison of the XRD patterns (Supplementary Fig. 19).

Molten-salt-shielding effect

To further broaden the substrate scope of our molten-nitrite method, we sought to isolate Dy atoms on metastable Cu_2O substrates. This process is particularly challenging because of the thermodynamic instability of Cu_2O at high temperatures in air. Surprisingly, we were able to obtain a Cu-based phase in different oxidation states simply by using different copper precursors with reducible counterions. Thus, we used copper citrate as a precursor for the synthesis of Dy_1/Cu_2O in air through the molten-salt system. The reason for the preservation of the Cu_2O matrix in heated air is that the molten nitrites act as barriers between the atmosphere and the as-generated NPs, effectively protecting the susceptible Cu_2O phase[36]. Figure 2c shows a schematic of the Dy_1/Cu_2O generation process. The corresponding digital photographs are listed in Supplementary Fig. 20 to visualize the molten-salt-shielding effect. The addition of the precursor immediately triggered the reaction, leading to the generation of Cu_2O, whereas part of the product was splashed onto the crucible wall (Supplementary Fig. 20b), ultimately turning into a black CuO phase due to oxidation (Supplementary Fig. 20c). By contrast, Dy_1/Cu_2O immersed in liquid molten salt retained its brick-red colour (Supplementary Fig. 20d). To circumvent the uncertainty of colour change, we conducted an in situ XRD experiment to validate the formation of Cu_2O in heated air, which clearly demonstrated the formation of the Cu_2O phase without the CuO phase (Supplementary Fig. 21). To further highlight the strong molten-salt-shielding effect, we prolonged the reaction time up to 6 h in air and monitored the product components by XRD patterns (Supplementary Fig. 22), which strongly substantiated that the Cu_2O phase can be effectively preserved in molten nitrites. So far, this strategy has been applied only to molten salts with relatively high eutectic points (above 700 °C), such as KBr (ref. 36) and NaCl–KCl (ref. 37). By contrast, our use of molten nitrites presents an alternative medium that enables the synthesis of sensitive materials at lower temperatures (400 °C) and avoids exposure to air.

Synthesis of Dy_1/Pt, Dy_1/Rh and Dy_1/Ir

To prove the generality of our molten nitrites, we further tried to proceed with the more challenging target of dispersing Ln(s) among noble metals. Previous studies show enhanced performance of Ln-doped noble metal electrocatalysts[5,6,8], but conventional synthesis remains challenging due to the distinct chemical properties between noble metals and Ln(s)[6]. Additionally, issues such as interparticle sintering[38] and air oxidation at high temperatures further complicate the synthesis process. Our molten-nitrite system effectively addresses these challenges through several key mechanisms: the L–F basicity facilitates the homogeneous dispersion of Ln elements, whereas near-melting-point nitrites enhance mass-diffusion resistance, thereby preventing NP agglomeration. Furthermore, molten-salt shielding, coupled with acetylacetonate precursors, enables the formation of metallic phases even in air, as acetylacetonate reduces metal ions into a metallic matrix in a manner similar to citrate during Dy_1/Cu_2O synthesis.

The EDS mapping images of Dy_1/Pt (Fig. 3a), Dy_1/Rh (Fig. 3c) and Dy_1/Ir (Fig. 3e) show that Dy is homogeneously distributed in these noble NPs. The coordination environment of Dy was revealed by EXAFS (Fig. 3g). The absence of the Dy–Dy shell supports the atomic dispersion of Dy, which is consistent with the wavelet-transform X-ray absorption fine structure analysis (Supplementary Fig. 23). The XANES analysis shown in Supplementary Fig. 24 reveals a positive shift in the absorption edge of Dy L_3 in each sample. This shift is consistent with the observations for Dy_1/CuO, Dy_1/Cu_2O and Dy_1/Cu.

The metallic nature of these NPs is confirmed by the distinct diffraction peaks observed in the XRD patterns, which are associated with Pt (Fig. 3b), Rh (Fig. 3d) and Ir (Fig. 3f). This confirms the effectiveness of the molten-salt-shielding effect in preventing metal oxidation. The TEM and high-resolution TEM images (Supplementary Figs. 25–27) reveal that the as-synthesized Dy_1/Pt, Dy_1/Rh and Dy_1/Ir are uniformly small, with sizes consistently less than 10 nm. In alignment with the abovementioned mechanisms, the small NP sizes are attributed to the use of near-melting-point nitrites with high viscosity, as thoroughly discussed in Supplementary Figs. 28–30 and Supplementary Note 9. The distinct molten-salt-shielding effect is further demonstrated by the oxidation of Ir in the absence of the nitrite shield (Supplementary Figs. 31 and 32 and Supplementary Note 10).

Other Ln SACs

To further validate the universality of molten nitrites for isolating Ln, we extended our synthesis approach to other Ln(s) and diverse substrates. The Ln doping levels in each sample were determined by inductively coupled plasma optical emission spectrometry (Supplementary Table 2). Specifically, we prepared Ln_1/Cu catalysts with various isolated Ln atoms (La, Pr, Nd, Sm, Eu, Gd, Tb, Ho, Er, Tm, Yb and Lu) by substituting dysprosium nitrate with the corresponding Ln nitrates. The atomically dispersed nature of each Ln among Cu is confirmed by the HAADF-STEM images (Fig. 4a) and EDS mappings (Supplementary Figs. 33–44). In addition, we demonstrated the simultaneous dispersion of La, Sm, Dy and Lu atoms into the Cu matrix (Supplementary Fig. 45). To further assess the general applicability of this method, we expanded the range of substrates including Dy_1/Y_2O_3, Dy_1/ZnO, Dy_1/Pd, Dy_1/AlO_x, Dy_1/RuO_2, Dy_1/SnO_2, Lu_1/FeO_x, Lu_1/Mn_3O_4 and Dy_1/C (the notation 'C' represents commercial carbon black). The homogeneous elemental distribution in the STEM-EDS mapping results confirmed the absence of small Ln(s) clusters or particles (Supplementary Figs. 46–54). The EXAFS spectra of all Ln SACs revealed single-atom structures similar to those of Dy_1/Cu, which indicated that the absence of an Ln–Ln coordination shell precluded the aggregation of Ln atoms (Fig. 4b, Supplementary Figs. 55–58 and Supplementary Note 11). Considering the potential corrosiveness of carbon substrates in molten salts, the detailed structure analysis of Dy_1/C is discussed in Supplementary Figs. 59 and 60 and Supplementary Note 12.

https://doi.org/10.1038/s41563-026-02492-y

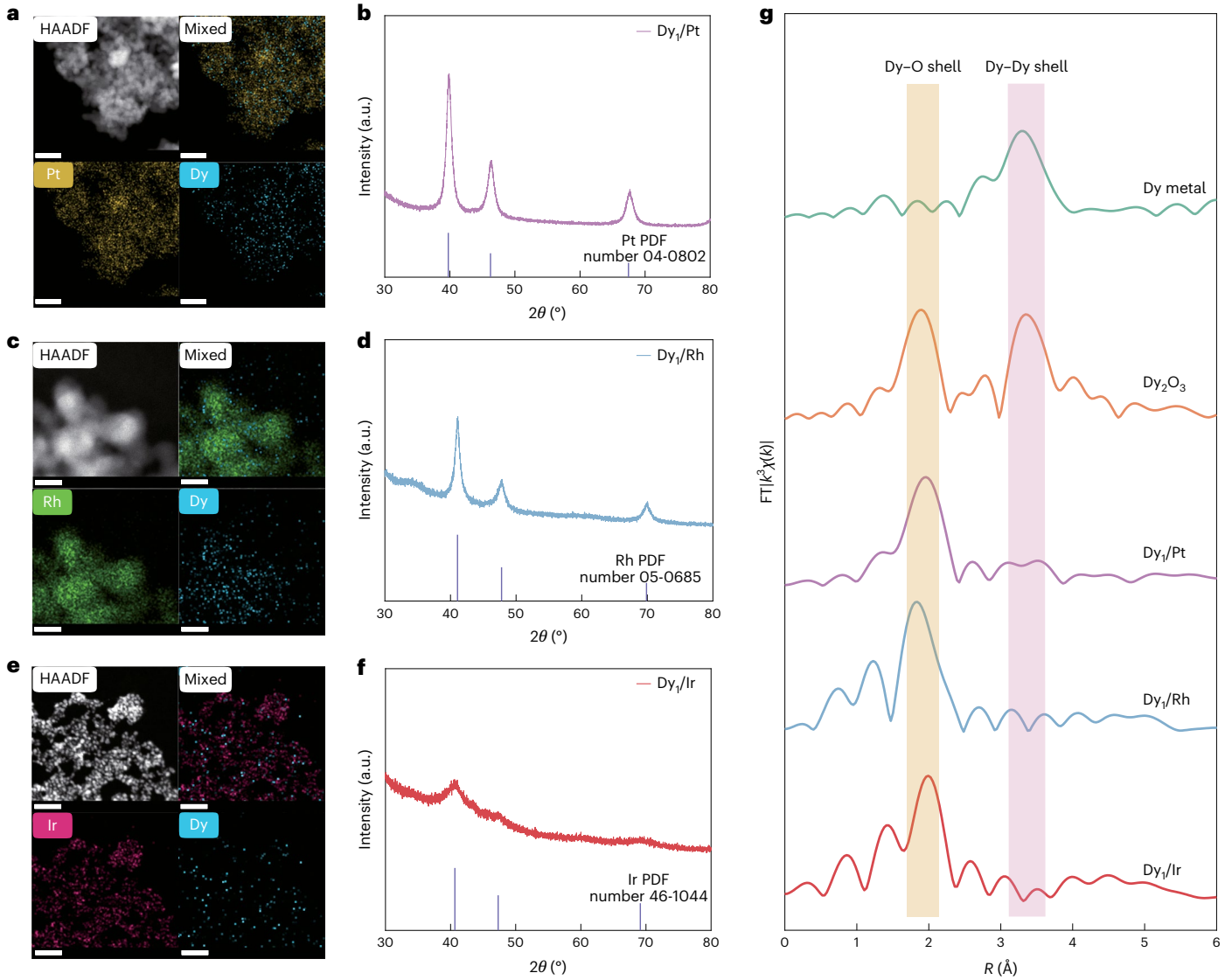

Fig. 3 | Synthesis of single Dy atoms on Pt, Rh and Ir NPs. a,**c**,**e**, EDS elemental mappings of Dy_1/Pt (**a**), Dy_1/Rh (**c**) and Dy_1/Ir (**e**). Scale bars, 20 nm (**a**,**e**); 5 nm (**c**). **b**,**d**,**f**, Powder XRD patterns of Dy_1/Pt (**b**), Dy_1/Rh (**d**) and Dy_1/Ir (**f**). The well-matched peaks with standard patterns indicate the generation of metallic Pt, Rh and Ir NPs in heated air. **g**, EXAFS analysis at the Dy L_3 edge of Dy_1/Pt, Dy_1/Rh and Dy_1/Ir.

Evaluation of catalytic performance

To assess the application potential of the Ln SACs synthesized from our molten-nitrite protocol, we investigated the CO_2 reduction reaction performance of Dy_1/Cu in a three-electrode flow cell reactor (Methods). As shown in Supplementary Fig. 61a,b, the selectivity of Cu with isolated Dy sites for C_{2+} products (C_2H_4, C_2H_5OH, CH_3COOH and C_3H_7OH) is greater than that of pure Cu. The Cu sites modified by Ln(s) clearly exhibit C_1 product suppression and favour C–C-coupling products (Supplementary Fig. 61c), consistent with previous reports[12].

To explore the versatility of our synthesis protocol, we subsequently focused on acidic HER as a model reaction and investigated the HER performance of Dy_1/Pt in Ar-saturated 0.5-M H_2SO_4. Compared with commercial Pt/C (27 mV) and Pt NPs (24 mV), Dy_1/Pt exhibited a lower overpotential of 20 mV in linear sweep voltammetry (LSV) tests at a current density of −10 mA cm^{-2} (Fig. 5a). Additionally, Dy_1/Pt requires only 33 mV to reach a current density of −100 mA cm^{-2}, whereas that of commercial Pt/C is 49 mV. The electrochemically active surface area (ECSA) obtained via hydrogen underpotential deposition from each sample is shown in Supplementary Fig. 62. The relatively low ECSA of Dy_1/Pt can potentially be ascribed to the obstructive and accumulative behaviour of nanocatalysts during the electrode assembly process. To evaluate the intrinsic activity of Dy_1/Pt, the ECSA-normalized LSV and turnover frequency were calculated, which indicated the superior intrinsic HER activity of Dy_1/Pt (Fig. 5b and Supplementary Fig. 63).

Measuring the Tafel slope is beneficial for determining the reaction mechanism in the acidic HER process. The Tafel slopes for Dy_1/Pt, Pt and commercial Pt/C were measured via a series of chronoamperometry tests (Fig. 5c). Dy_1/Pt exhibited a lower Tafel slope (30.9 mV dec^{-1}) than Pt (44.8 mV dec^{-1}) and commercial Pt/C (32.5 mV dec^{-1}), implying that its more rapid HER kinetics were attributed to the Volmer–Tafel mechanism. In addition, Dy_1/Pt exhibited satisfactory stability under continuous electrolysis (Fig. 5d). At −10 mA cm^{-2}, Dy_1/Pt shows no appreciable potential loss for more than 200 h, comparable with the performance of mature commercial Pt/C catalysts used widely in industrial water electrolysis. We also benchmarked the intrinsic activity and stability of Dy_1/Pt against existing SACs reported for the acidic HER. As summarized in Supplementary Table 3, compared with most known SAC systems, Dy_1/Pt exhibits superior or comparable performance metrics,

https://doi.org/10.1038/s41563-026-02492-y

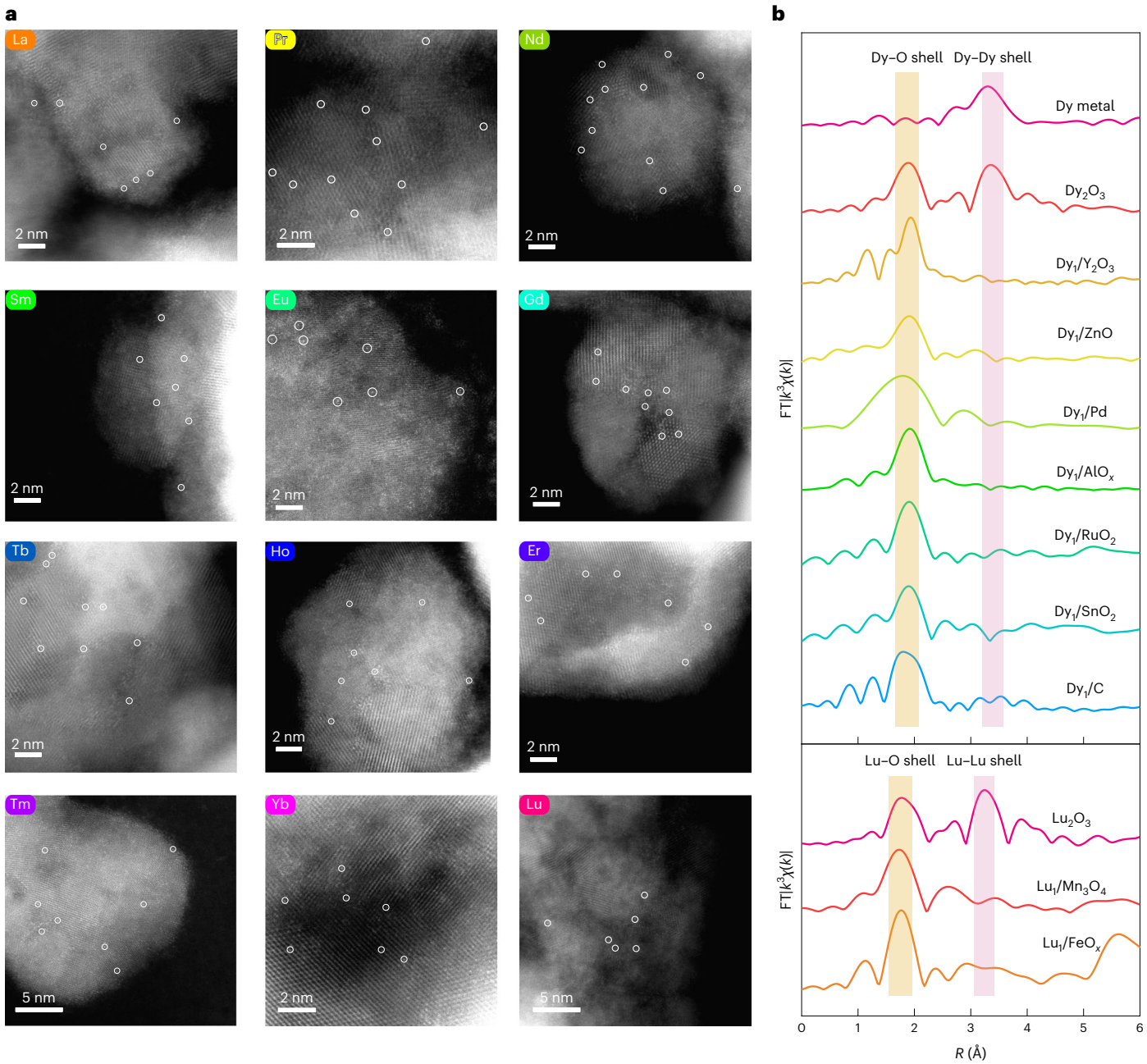

Fig. 4 | Generality of molten nitrites for synthesizing Ln SACs. a, HAADF-STEM images of Ln_1/Cu (Ln = La, Pr, Nd, Sm, Eu, Gd, Tb, Ho, Er, Tm, Yb, Lu). **b**, Dispersing Ln(s) within different substrates, including Dy for Y_2O_3, ZnO, Pd, AlO_x, RuO_2, SnO_2, commercial XC-72 and Lu for Mn_3O_4 and FeO_x.

including overpotential, Tafel slope and long-term stability. This highlights the excellent intrinsic catalytic properties of Dy_1/Pt for the acidic HER. Density functional theory calculations further confirm that Dy_1/Pt exhibits a lower H_2 formation energy barrier than Pt (Supplementary Figs. 64–66, Supplementary Note 13 and Supplementary Table 4). Moreover, when assembled into a proton exchange membrane water electrolysis (PEMWE) device (Fig. 5e), our Dy_1/Pt exhibited a lower operating voltage than commercial Pt/C at a controlled operation temperature of 80 °C (identical Pt loading for the PEMWE test; Supplementary Fig. 67), demonstrating its practical application potential. For ampere-level water electrolysis, Dy_1/Pt maintained a stable voltage without obvious activity decay over 100 h at 80 °C (Supplementary Fig. 68). Importantly, it sustained a low cell voltage at 25 °C and exhibited stable operation for more than 1,700 h at 200 mA cm^{-2} (Fig. 5f). Post-operation analyses further confirmed structural integrity and single-atom persistence. TEM of the PEMWE-tested catalyst (Supplementary Fig. 69a) showed that Dy_1/Pt retained its original NP morphology. STEM-EDS elemental mapping (Supplementary Fig. 69b–d) revealed uniform Pt and Dy distributions without detectable Dy aggregation, indicating that Dy remained atomically dispersed during device operation. Collectively, these results highlight Dy_1/Pt as a durable, intrinsically active acidic HER catalyst and underscore molten nitrites as a versatile platform for developing practical energy conversion catalysts.

In summary, we introduced a general molten-nitrite system for the synthesis of Ln SACs. The proposed molten-nitrite system is proven to be general and efficient for generating Ln-doped oxides with different valences, Ln-isolated metallic NPs and Ln-isolated carbon-based substrates. We further elucidate the intrinsic synthesis mechanisms involved, including L–F basicity, mass-diffusion effects

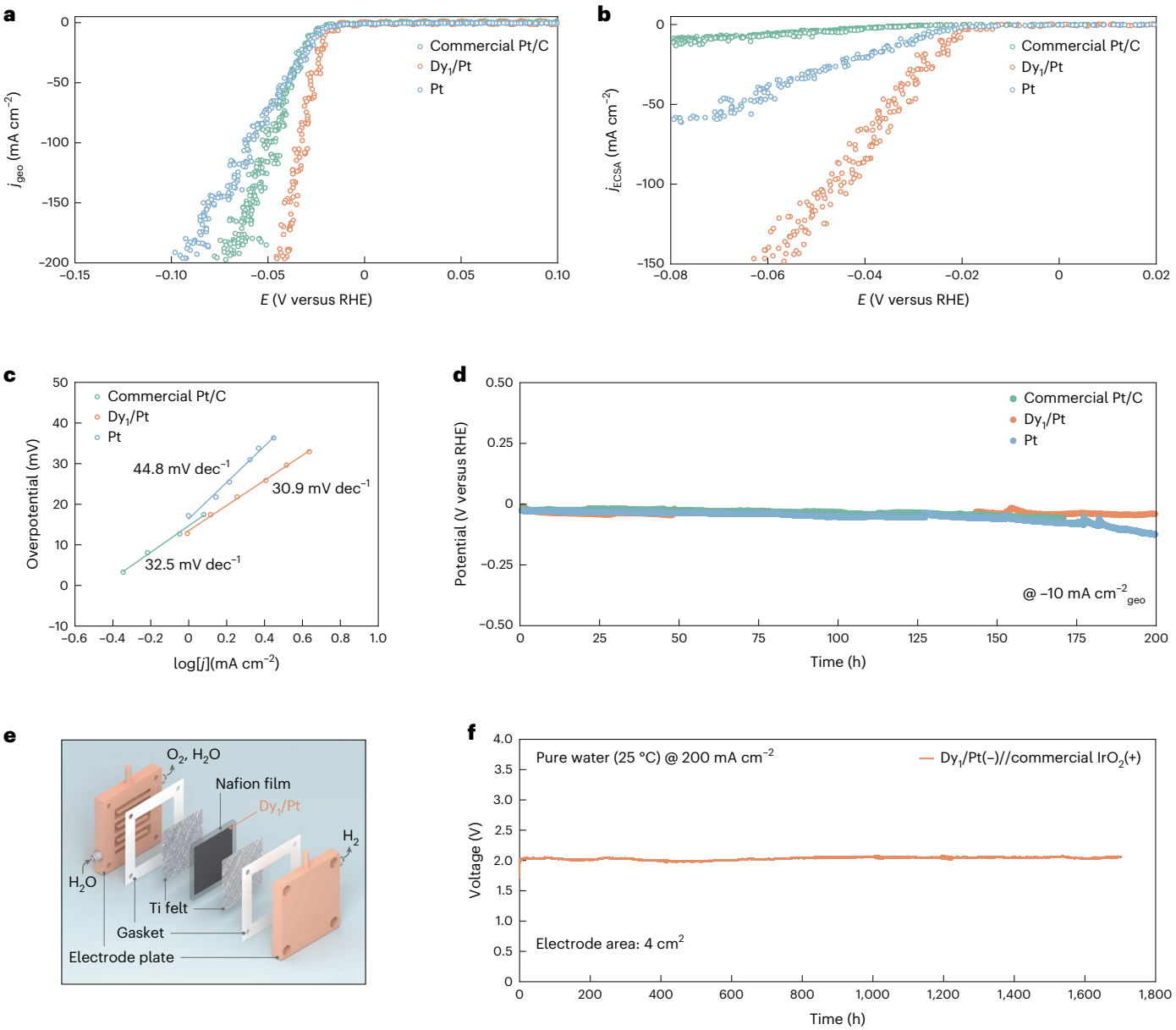

Fig. 5 | HER performance of Dy_1/Pt in 0.5-M H_2SO_4. **a**, LSV curves of Dy_1/Pt and references normalized by the geometric area. **b**, LSV curves of Dy_1/Pt and references normalized by the ECSA. **c**, Tafel slopes of Dy_1/Pt and the reference materials. **d**, Stability test of the time-dependent potential of Dy_1/Pt and reference materials under consistent conditions of −10 mA cm^{-2} and 0.5-M H_2SO_4. **e**, PEMWE demonstration using commercial IrO_2 as the anode catalyst. **f**, Chronopotentiometry stability test was performed at 200 mA cm^{-2} under a controlled temperature of 25 °C.

and molten-salt-shielding effects. These mechanisms facilitate the optimization of synthesis protocols and their extension to various target products. As a demonstration, Dy_1/Pt exhibits notable acidic HER performance, underscoring the potential of the molten-nitrite system for constructing Ln SACs. In a broader context, our molten nitrites offer prominent features: a tunable chemical composition that can be precisely tailored to diverse synthesis targets, compatibility across a large scope of products without organic containment and synthesis accessibility through simple and commercial equipment. Beyond the Ln SACs reported here, broader elemental selections and tailored nanostructures can be realized through molten-nitrite engineering in the future.

Online content

Any methods, additional references, Nature Portfolio reporting summaries, source data, extended data, supplementary information, acknowledgements, peer review information; details of author contributions and competing interests; and statements of data and code availability are available at https://doi.org/10.1038/s41563-026-02492-y.

References

1. Li, C. et al. Rare earth-based nanomaterials in electrocatalysis. *Coord. Chem. Rev.* **489**, 215204 (2023).
2. Lucas, J. et al. Rare earths: science, technology, production and use. *MRS Bull.* **40**, 452–453 (2015).
3. Wang, X. et al. Embedding oxophilic rare-earth single atom in platinum nanoclusters for efficient hydrogen electro-oxidation. *Nat. Commun.* **14**, 3767 (2023).
4. Feng, J. et al. CO_2 electrolysis to multi-carbon products in strong acid at ampere-current levels on La-Cu spheres with channels. *Nat. Commun.* **15**, 4821 (2024).

5. Escudero-Escribano, M. et al. Pt_5Gd as a highly active and stable catalyst for oxygen electroreduction. *J. Am. Chem. Soc.* **134**, 16476–16479 (2012).
6. Escudero-Escribano, M. et al. Tuning the activity of Pt alloy electrocatalysts by means of the lanthanide contraction. *Science* **352**, 73–76 (2016).
7. Li, M. et al. Oxophilic Tm-sites in MoS_2 trigger thermodynamic spontaneous water dissociation for enhanced hydrogen evolution. *Adv. Energy Mater.* **14**, 2401716 (2024).
8. Mao, Q. et al. High-density rare-earth single-atom-triggered unconventional transition of adsorption configuration on La_1Pd monatomic alloy metallene for sustainable electrocatalytic alkynol semi-hydrogenation. *Adv. Funct. Mater.* **34**, 2404648 (2024).
9. Li, L. et al. Lanthanide-regulating Ru-O covalency optimizes acidic oxygen evolution electrocatalysis. *Nat. Commun.* **15**, 4974 (2024).
10. Zhang, S. et al. Lanthanide electronic perturbation in Pt-Ln (La, Ce, Pr and Nd) alloys for enhanced methanol oxidation reaction activity. *Energy Environ. Sci.* **14**, 5911–5918 (2021).
11. Sun, Y. et al. Boosting CO_2 electroreduction to C_2H_4 via unconventional hybridization: high-order $Ce^{4+}4f$ and O2*p* interaction in Ce-Cu_2O for stabilizing Cu^+. *ACS Nano* **17**, 13974–13984 (2023).
12. Feng, J. et al. Improving CO_2-to-C_{2+} product electroreduction efficiency via atomic lanthanide dopant-induced tensile-strained CuO_x catalysts. *J. Am. Chem. Soc.* **145**, 9857–9866 (2023).
13. Xu, J. et al. Ultrathin 2D rare-earth nanomaterials: compositions, syntheses, and applications. *Adv. Mater.* **32**, 1806461 (2020).
14. Hu, Y. et al. Synthesis of Pt-rare earth metal nanoalloys. *J. Am. Chem. Soc.* **142**, 953–961 (2020).
15. Santos, D. M. F. et al. Platinum–rare earth electrodes for hydrogen evolution in alkaline water electrolysis. *Int. J. Hydrogen Energy* **38**, 3137–3145 (2013).
16. Hu, Y. et al. Mechanistic insights into the synthesis of platinum–rare earth metal nanoalloys by a solid-state chemical route. *Chem. Mater.* **33**, 535–546 (2021).
17. Kanady, J. S. et al. Synthesis of Pt_3Y and other early–late intermetallic nanoparticles by way of a molten reducing agent. *J. Am. Chem. Soc.* **139**, 5672–5675 (2017).
18. Jiang, Y. et al. Molten salt synthesis of carbon-supported Pt-rare earth metal nanoalloy catalysts for oxygen reduction reaction. *RSC Adv.* **12**, 4805–4812 (2022).
19. Wang, X., Tang, Y., Lee, J.-M. & Fu, G. Recent advances in rare-earth-based materials for electrocatalysis. *Chem. Catal.* **2**, 967–1008 (2022).
20. Peera, S. G., Lee, T. G. & Sahu, A. K. Pt-rare earth metal alloy/metal oxide catalysts for oxygen reduction and alcohol oxidation reactions: an overview. *Sustain. Energ. Fuels* **3**, 1866–1891 (2019).
21. Nitopi, S. et al. Progress and perspectives of electrochemical CO_2 reduction on copper in aqueous electrolyte. *Chem. Rev.* **119**, 7610–7672 (2019).
22. Ma, W. et al. Electrocatalytic reduction of CO_2 and CO to multi-carbon compounds over Cu-based catalysts. *Chem. Soc. Rev.* **50**, 12897–12914 (2021).
23. Lin, Y. X. et al. Boosting selective nitrogen reduction to ammonia on electron-deficient copper nanoparticles. *Nat. Commun.* **10**, 4380 (2019).
24. Zhang, R. et al. Electrochemical nitrate reduction to ammonia using copper-based electrocatalysts. *Next Energy* **4**, 100125 (2024).
25. Li, Y. et al. Advancements in transition bimetal catalysts for electrochemical 5-hydroxymethylfurfural (HMF) oxidation. *J. Energy Chem.* **98**, 24–46 (2024).
26. Zheng, T. et al. Copper-catalysed exclusive CO_2 to pure formic acid conversion via single-atom alloying. *Nat. Nanotechnol.* **16**, 1386–1393 (2021).
27. Li, J. et al. Selective CO_2 electrolysis to CO using isolated antimony alloyed copper. *Nat. Commun.* **14**, 340 (2023).
28. LaMer, V. K. & Dinegar, R. H. Theory, production and mechanism of formation of monodispersed hydrosols. *J. Am. Chem. Soc.* **72**, 4847–4854 (1950).
29. Li, T. et al. Low-temperature molten salt synthesis for ligand-free transition metal oxide nanoparticles. *ACS Appl. Energy Mater.* **3**, 3984–3990 (2020).
30. Jansons, A. W., Koskela, K. M., Crockett, B. M. & Hutchison, J. E. Transition metal-doped metal oxide nanocrystals: efficient substitutional doping through a continuous growth process. *Chem. Mater.* **29**, 8167–8176 (2017).
31. Kerridge, D. H. & Shakir, W. M. Molten lithium nitrate-potassium nitrate eutectic: the reaction of tin(II) chloride. *Thermochim. Acta* **136**, 149–152 (1988).
32. Hu, C. et al. Misoriented high-entropy iridium ruthenium oxide for acidic water splitting. *Sci. Adv.* **9**, eadf9144 (2023).
33. Vreeland, E. C. et al. Enhanced nanoparticle size control by extending LaMer's mechanism. *Chem. Mater.* **27**, 6059–6066 (2015).
34. Hayashi, Y., Kimura, T. & Yamaguchi, T. Preparation of rod-shaped $BaTiO_3$ powder. *J. Mater. Sci.* **21**, 757–762 (1986).
35. Zhao, D. et al. On the viscosity of molten salts and molten salt mixtures and its temperature dependence. *J. Energy Storage* **61**, 106707 (2023).
36. Dash, A., Vaßen, R., Guillon, O. & Gonzalez-Julian, J. Molten salt shielded synthesis of oxidation prone materials in air. *Nat. Mater.* **18**, 465–470 (2019).
37. Dash, A. et al. Synthesis of Ti_3SiC_2 MAX phase powder by a molten salt shielded synthesis (MS^3) method in air. *J. Eur. Ceram. Soc.* **39**, 3651–3659 (2019).
38. Dai, Y. et al. The physical chemistry and materials science behind sinter-resistant catalysts. *Chem. Soc. Rev.* **47**, 4314–4331 (2018).

Methods

Synthesis of Dy_1/CuO

First, 0.2268 g of $Dy(NO_3)_3{\cdot}6H_2O$ was dissolved in 3 ml of deionized (DI) water to obtain the Dy solution. Then, 50 µl of Dy solution and 0.2 g of $Cu(NO_3)_2{\cdot}3H_2O$ were added to 100 µl of DI water. The above solution was intensively vibrated by a vortex mixer for 5 min to generate a transparent, homogeneous solution as the precursor solution (the Dy–Cu precursor). Here 2.24 g of $NaNO_2$ and 2.76 g of KNO_2 were mixed in a crucible and heated at 400 °C for 60 min to form a clear yellow liquid in an air muffle furnace. Then, the Dy–Cu precursor solution was directly injected into the molten nitrites and held for 30 min. After the reaction, the crucible was removed from the furnace and naturally cooled to room temperature. The nitrites were removed by simple washing with DI water and collected by centrifugation at 12,000 r.p.m. (~16,100*g*) for 5 min for five times. The generated Dy_1/CuO sample was dried under a vacuum.

Synthesis of Dy_1/Y_2O_3, Dy_1/ZnO, Dy_1/Pd, Dy_1/AlO_x, Dy_1/SnO_2, Dy_1/RuO_2, Lu_1/Mn_3O_4 and Lu_1/FeO_x

The synthesis followed the procedure of Dy_1/CuO using 0.2 g of the respective precursors: $Y(NO_3)_3{\cdot}6H_2O$, $Zn(NO_3)_2{\cdot}6H_2O$, $Pd(NO_3)_2{\cdot}2H_2O$, $Al(NO_3)_3{\cdot}9H_2O$, $SnCl_4{\cdot}5H_2O$, $RuCl_3{\cdot}xH_2O$, $Mn(NO_3)_2{\cdot}4H_2O$ and $Fe(NO_3)_3{\cdot}9H_2O$. The Dy solution was identical to that used in Dy_1/CuO. The volume of Dy solution added was 32.0 µl for Dy_1/Y_2O_3, 40.6 µl for Dy_1/ZnO, 45.3 µl for Dy_1/Pd, 32.2 µl for Dy_1/AlO_x and 34.5 µl for Dy_1/SnO_2. The Dy solution and the corresponding substrate precursor were dissolved within 100 µl of DI water. As for Dy_1/RuO_2, 46.2 µl of Dy solution and 300 µl of DI water were used.

The used Lu solution for Lu_1/Mn_3O_4 and Lu_1/FeO_x was prepared by dissolving 0.1934 g of $Lu(NO_3)_3{\cdot}6H_2O$ in 3 ml of DI water. The volume of the Lu solution added was 56.4 µl for Lu_1/Mn_3O_4 and 35.1 µl for Lu_1/FeO_x. The Lu solution and the corresponding substrate precursor were dissolved within 100 µl of DI water.

Synthesis of Dy_1/C

Here 2 g of commercial XC-72 carbon black was fully washed and activated with 100 ml of 9-M HNO_3 under reflux at 80 °C. Then, the carbon black was mixed with dysprosium nitrate as a precursor for molten-salt synthesis. Typically, 200 mg of washed carbon black was immersed in 50 ml of 5 mg ml^{-1} of $Dy(NO_3)_3{\cdot}6H_2O$ solution under vigorous stirring overnight. After thoroughly removing the unabsorbed dysprosium nitrite, 50 mg of dry Dy-treated carbon black was added to the premelted molten nitrites composed of 2.24 g of $NaNO_2$ and 2.76 g of KNO_2 at 400 °C and held for 30 min. The purification step was the same as that for Dy_1/CuO.

Synthesis of Dy_1/Cu_2O

The synthesis of Dy_1/Cu_2O followed the same procedures as those used for Dy_1/CuO, except that 300 µl of saturated Na_3CA solution, 50 µl of Dy solution and 0.2 g of $Cu(NO_3)_2{\cdot}3H_2O$ were used as the Dy–Cu precursor.

Synthesis of Dy_1/Cu

Here 8 mg of Dy_1/CuO, 16 µl of Nafion and 1 ml of isopropanol were mixed and sonicated for 1 h. After that, the ink was airbrushed onto a 1.13-cm^2 glass carbon surface as an electrode. Dy_1/CuO was reduced at −1.2 V versus RHE in a CO_2-saturated 0.5-M $KHCO_3$ solution for 60 min to fully reduce Dy_1/CuO into Dy_1/Cu.

Synthesis of Ln_1/Cu

Synthesis of Ln_1/Cu (Ln = La, Pr, Nd, Sm, Eu, Gd, Tb, Ho, Er, Tm, Yb, Lu) followed the same procedure as Dy_1/Cu but simply replaced $Dy(NO_3)_3{\cdot}6H_2O$ with equimolar Ln nitrates; the precursor of LaSmDyLu-Cu was obtained by simply mixing several Ln nitrates.

Synthesis of Dy_1/Pt

Here 47 mg of $Dy(acac)_3$ was dissolved in 20 ml of acetone. A total of 0.5 ml of the above mixture and 5 ml of acetone were added to dissolve 50 mg of $Pt(acac)_2$ to generate a transparent, homogeneous solution via a vortex mixer. The mixture was quickly evaporated in an 80 °C water bath to obtain a well-mixed Dy–Pt precursor. The precursor was fully ground with 5 g of $NaNO_2$ in a crucible and directly placed into a 270 °C muffle furnace without any gas protection. The $NaNO_2$ was semimelted and maintained for 90 min before it was naturally cooled to room temperature. The nitrites were removed by simple washing with DI water and collected by centrifugation at 12,000 r.p.m. (~16,100*g*) for 5 min for five times. The generated Dy_1/Pt sample was dried under a vacuum.

Synthesis of Dy_1/Rh

Similar to the case of Dy_1/Pt, 47 mg of $Dy(acac)_3$ was dissolved in 20 ml of acetone. A total of 0.98 ml of the above mixture and 20 ml of acetone were added to dissolve 100 mg of $Rh(acac)_3$ to generate a transparent, homogeneous solution via a vortex mixer. The mixture was also quickly evaporated in an 80 °C water bath (operating in a fume hood with reinforced glasses) to obtain a well-mixed Dy–Rh precursor. The precursor was fully ground with 4 g of KBr, which acted as an inert buffer layer in the next step. The decomposition temperature of $Rh(acac)_3$ is higher than that of $Pt(acac)_2$. Thus, 9.25 g of KNO_2 and 1.50 g of $NaNO_2$ were premelted at 400 °C to elevate the melting point. The above nitrites are then mixed with the above precursor at 350 °C in a crucible. Without any protective gas, the crucible was kept for 90 min before being naturally cooled to room temperature. The salts were removed by simple washing with DI water and collected by centrifugation at 12,000 r.p.m. (~16,100*g*) for 5 min for five times. The generated Dy_1/Rh sample was dried under a vacuum.

Synthesis of Dy_1/Ir

Similar to Dy_1/Rh, 47 mg of $Dy(acac)_3$ was dissolved in 20 ml of acetone. A total of 0.80 ml of the above solution and 10 ml of acetone were added to dissolve 100 mg of $Ir(acac)_3$ to generate a transparent, homogeneous solution via a vortex mixer. The mixture was also quickly evaporated in an 80 °C water bath to obtain a well-mixed Dy–Ir precursor. The next step is the same as that in Dy_1/Rh.

Role of KBr in synthesis

KBr introduced in the process of synthesizing Dy_1/Rh and Dy_1/Ir is an inert cushion layer, which prevents precursors with a fluffy texture from blowing away when mixed with molten nitrites. In addition, the coarse and squishy KNO_2 granules were difficult to mechanically mill, impeding our ability to premix nitrites and precursors. Previous studies have reported that KBr serves as an effective heating bed for synthesizing chemically vulnerable materials[36]. Thus, we selected KBr for its suitable mechanical properties, ultrahigh melting point and inert chemical performance as the buffer layer in our work. For the sake of rigour, we also directly heated the Dy–Ir precursor with a KBr buffer layer at 350 °C to demonstrate the necessity of molten nitrites. In this study, we obtained only oxidized Ir agglomerates without a Dy signal in the EDS mapping results. Thus, the L–F basicity, mass-diffusion resistance and salt-shielding effect of molten nitrites are critical.

HER performance. The electrochemical measurements were conducted in a typical H cell (50 ml) with a lid at room temperature. The applied potentials were controlled by an electrochemical workstation (BioLogic VMP3). Here 30 ml of Ar-saturated 0.5-M H_2SO_4 solution was used as both anolyte and catholyte. A graphite rod electrode was used as the counter electrode, and a calibrated saturated mercurous sulfate electrode (Hg/Hg_2SO_4) was used as the reference electrode. The potentials obtained in three-electrode systems were converted to the RHE scale (with 100% *iR* compensation). The working electrode

was prepared as follows: 10 mg of Dy_1/Pt or ~16.6 mg of Pt/C was dispersed in 10 ml of isopropanol containing 200 µl of Nafion solution under ultrasonication. A total of 113 µl of ink was dropped onto a glass carbon electrode (0.6 cm in diameter) for further tests. The LSV experiments were conducted with a scan rate of 5 mV s^{-1} in the range of −0.5 to −1.2 V versus the reference electrode. The hydrogen underpotential deposition experiment was performed with a scan rate of 50 mV s^{-1} in the range of −0.15 to −0.69 V versus the reference electrode. The H-cell stability data were collected at −10 mA cm^{-2} in chronopotentiometry mode. Considering potential catalyst shedding, we sprayed 1 ml of ink over 1 cm^2 of carbon paper (Toray TGP-H060) as a working electrode. To obtain the uncompensated resistance, potentiostatic electrochemical impedance spectroscopy experiments were conducted in the frequency range of 10 mHz to 200 kHz at the open-circuit potential after the tests. For reference electrode calibration, the reversible hydrogen electrode we used consists of a Pt wire as a counter electrode, the determined reference electrode and a Pt foil electrode covered with Pt black powder. The electrolyte used in other electrochemical tests was selected as the electrolyte for calibration. The pure hydrogen flow rate was maintained at 50 s.c.c.m. (monitored by an Alicat Scientific mass flow controller) for saturation to achieve 1-atm H_2 partial pressure. The CV data at a scan rate of 1 mV s^{-1} indicate that the calibrated Hg/Hg_2SO_4 potential is 0.691 V versus RHE.

The conversion formula to the RHE scale is as follows:

$$E(\text{versus, RHE}) = E(\text{versus ref.}) - iR_{\text{compensation}} + 0.691V.$$

The equation for calculating the ECSA (cm^2) is as follows:

$$\text{ECSA} = \frac{1,000 \times S_{\text{H}}}{Q_{\text{H}} \times V}.$$

where S_{H} represents the area of the H* oxidation desorption peak (mA V). V represents the scan rate (mV s^{-1}). Q_{H} is the H adsorption/desorption charge density on polycrystalline Pt, with a value of 0.21 (mC cm^{-2}) according to ref. 39.

The equation formula of the turnover frequency (s^{-1}) is as follows:

$$\text{TOF} = \frac{I}{2 \times Q_{\text{H}} \times \text{ECSA}}.$$

Moreover, the Tafel slope is calculated by linear fitting of the following equation:

$$\eta = b \log[-j] + a.$$

CO_2 reduction reaction performance. The three-electrode performance was collected using a conventional flow cell. For the fabrication of the gas diffusion electrode as the cathode, 12 mg of catalyst was dispersed in 1.5 ml of isopropanol containing 24 µl of Nafion under ultrasonication. The obtained ink was sprayed onto a gas diffusion layer (YLS-30T) using an airbrush and dried on a hot plate at 80 °C. Commercial Hg/HgO with 1-M KOH as the filling solution was used as the reference electrode, and a piece of Ni foam was used as the anode. The 1-M KOH solution circulated at 2.2 ml min^{-1} was used as the cathode electrolyte. The geometric area of the catalyst exposed to the electrolyte was 0.75 cm^2. The CO_2 flow rate (50 s.c.c.m.) was monitored by an Alicat Scientific mass flow controller.

The gas products were quantified by a gas chromatograph (Perkin Elmer Clarus 690) equipped with a thermal conductivity detector and a flame ionization detector. The liquid products in the CO_2 reduction reaction were quantified by a 600-MHz nuclear magnetic resonance spectrometer (Bruker AVANCE NEO) in deuteroxide. Before the test, 600 µl of the electrolyte containing the liquid products was mixed with 100 µl of D_2O (Sigma-Aldrich, 99.9%) and 0.1 µl of dimethyl sulfoxide (Sigma-Aldrich, 99.9%).

Proton exchange membrane water electrolyser. Here 5 mg of Dy_1/Pt or ~8.3 mg of Pt/C (Hispec Pt/C, Sinero) was uniformly dispersed in 50 µl of Nafion and 5 ml of isopropanol under ultrasonication. The obtained ink was then sprayed over the Nafion membrane (one side was loaded with hot-pressed commercial IrO_2). The membrane was subsequently hot pressed under 5-MPa pressure for 2 min at 100 °C. Carbon paper (Toray TGP-H060) and Ti foam were used as gas diffusion layers at the cathode and anode sides, respectively. The proton exchange membrane electrolyser was operated at 25 °C with a temperature controller using pure water as the flow electrolyte. The flow rate was 2.5 ml min^{-1} for the 0.8-A operation and 15 ml min^{-1} for the 4.0-A test.

Additional methods. A list of used chemicals, details of materials characterizations and computational methods are provided in Supplementary Information.

Data availability

All data generated or analysed during this study are included in the article and its Supplementary Information, and are also available from the corresponding author upon request. Source data are provided with this paper.

References

39. Chen, J. et al. Diversity of platinum-sites at platinum/fullerene interface accelerates alkaline hydrogen evolution. *Nat. Commun.* **14**, 1711 (2023).

Acknowledgements

C.X. acknowledges the National Key Research and Development Program of China (2024YFB4105700), the Scientific Research Innovation Capability Support Project for Young Faculty (SRICSPYF-ZY2025052), the Natural Science Foundation of Sichuan Province (2025NSFJQ0017) and the University of Electronic Science and Technology of China (ZYGX2025TS001). T.Z. acknowledges NSFC (22278067 and 22322201). X.L. acknowledges NSFC (22475030) and the Natural Science Foundation of Sichuan Province (2024NSFSC1107). Q.J. acknowledges NSFC (22405035) and the Natural Science Foundation of Sichuan Province (2024NSFSC1104). We appreciate the Analysis and Testing Center, University of Electronic Science and Technology of China, for their technical support, especially Y. Hu and J. Li with regard to XRD and HAADF-STEM, respectively. We thank beamline BL11B (31124.02.SSRF.BL11B) of the Shanghai Synchrotron Radiation Facility for providing the beamtime. We appreciate the discussion with C. Guo from SUPCON Technology for the theoretical computations in this work.

Author contributions

The project was conceptualized and supervised by C.X. H.W. conducted all the experiments with help from the other authors. H.W. carried out all the sample syntheses. H.W., H.Z. and Q.Z. performed the electrochemical tests. S.H. helped with the electron microscopy. H.W., J.L. and X.Z. performed the ex situ measurements. H.W. and Q.G. conducted the X-ray absorption fine structure measurements. C.L., X.L. and Y.Z. helped with the statistical analysis. C.L., X.Z., Q.Z. and J.L. provided useful discussion on this work. J.Z. helped with the design of the mechanism experiments. Y.J. designed the figures in the paper. H.W., C.L., T.Z., Q.J. and C.X. wrote and revised the paper.

Competing interests

The authors declare no competing interests.

Additional information

Supplementary information The online version contains supplementary material available at https://doi.org/10.1038/s41563-026-02492-y.

Correspondence and requests for materials should be addressed to Chuan Xia.

Peer review information *Nature Materials* thanks Wolfgang Schmidt, Deli Wang and the other, anonymous, reviewer(s) for their contribution to the peer review of this work.